

Enhanced Spin Hall Ratio in Two-Dimensional III-V Semiconductors

Jiaqi Zhou*

*Institute of Condensed Matter and Nanosciences (IMCN),
Université catholique de Louvain (UCLouvain), B-1348, Louvain-la-Neuve, Belgium*

Samuel Ponce†

*European Theoretical Spectroscopy Facility and
Institute of Condensed Matter and Nanosciences (IMCN),
Université catholique de Louvain (UCLouvain), B-1348, Louvain-la-Neuve, Belgium*

Jean-Christophe Charlier‡

*Institute of Condensed Matter and Nanosciences (IMCN),
Université catholique de Louvain (UCLouvain), B-1348, Louvain-la-Neuve, Belgium*

(Dated: August 29, 2023)

Spin Hall effect plays a critical role in spintronics since it can convert charge current to spin current. Using state-of-the-art *ab initio* calculations including quadrupole and spin-orbit coupling, the charge and spin transports have been investigated in pristine and doped two-dimensional III-V semiconductors. Valence bands induce a strong scattering which limits charge conductivity in the hole-doped system, where spin Hall conductivity is enhanced by the spin-orbit splitting, yielding an ultrahigh spin Hall ratio $\xi \approx 0.9$ in GaAs monolayer at room temperature.

Introduction – The strength of Hall effect can be denoted by $\beta = \tan(\theta_H) = E_H/E$ where θ_H is the Hall angle, E_H is the transverse Hall field, and E is the longitudinal electric field [1]. Correspondingly, the strength of spin Hall effect (SHE) can be given by the spin Hall ratio (SHR) as $\xi = \tan(\theta_{SH}) = \frac{2e}{\hbar} \left| \frac{J_s}{J_c} \right|$ where θ_{SH} is the spin Hall angle, J_s is the transverse spin Hall current density, and J_c is the longitudinal charge current density. SHR is often used as a proxy to indicate the charge-to-spin conversion efficiency which is crucial for low-power-consumption spintronic applications [2, 3]. Indeed, when θ_{SH} is small, the first-order Taylor polynomial gives $\xi \approx \theta_{SH}$, which is a good approximation for the bulk semiconductors and metals where $\xi \sim 0.01$ [4–6]. Recently, enhanced SHR has been revealed in various two-dimensional (2D) van der Waals materials with strong spin-orbit coupling (SOC). Huge SHRs over 10 are reported in topological insulators [7, 8] while large $\text{SHR} \sim 0.5$ in MoTe₂ and WTe₂ Weyl semimetals have also been theoretically and experimentally identified [9–12]. Besides, the MoS₂ monolayer can exhibit $\xi = 0.14$ induced by the Rashba-Edelstein effect [13]. Noted that large ξ will break the approximation $\xi \approx \theta_{SH}$ and therefore the spin Hall ratio rather than the spin Hall angle should be used to denote the ratio of spin current to charge current. In addition to the SHR enhancement, 2D materials also provide a platform for unconventional properties which are intertwined with their underlying structural symmetry [14]. 2D semiconductors composed of heavy atoms are promising for SHE: Strong SOC can induce a large spin Hall conductivity (SHC), and the broken-symmetry structure enables the unconventional spin Hall current [15, 16]. In the case of semiconductors, doping is another degree of freedom to effectively control the transport behavior.

Although charge transport and SHC have been separately in-

vestigated in 2D materials [17–21], the study of SHR remains elusive due to the entanglement of electron-phonon interaction [22, 23] and SOC [2, 3]. In this Letter, we report the spin Hall ratio in III-V monolayers (MX, M=Ga, In, and X = P, As, Sb) using density functional theory [24], density functional perturbation theory [25], and Wannier functions [26]. The electron-phonon coupling, quadrupole correction [27], Berry connection [28], and SOC are considered in the room-temperature calculations. The broken-inversion symmetry and the strong SOC induce a Rashba splitting in the conduction bands, making the band edge analogous to a single valley at the center of Brillouin zone. The weak intravalley scattering results in exceptional electron mobilities over 1000 cm²/Vs along with high conductivities over 50 e²/h in the electron-doped systems, where a universal SHC of $-0.5 (\hbar/2e)e^2/h$ has been identified as a hallmark of Rashba system. In contrast, the hole-doped mobilities are significantly suppressed by the strong intervalley scattering, while high SHCs over $2 (\hbar/2e)e^2/h$ occur due to the strong spin-orbit splitting, yielding an ultrahigh SHR of $\xi \approx 0.9$ in GaAs monolayer.

Methods and models – We compute the charge transport properties by solving the iterative Boltzmann transport equation [29] and the spin Hall conductivity using the Kubo formula [30] as implemented in the EPW [31, 32], WANNIER90 [33], QUANTUM ESPRESSO [34], and ABINIT [35] codes considering SOC, 2D Coulomb truncation [36], and gauge-covariant quadrupolar contributions [37]. Additional details are provided in Section S1 of the supplementary information (SI) [38]. Pristine III-V monolayers are semiconductors which crystallize in a low-buckled honeycomb structure [39]. Details of the relaxed atomic structures, effective masses, Rashba constants, electrostatic properties, densities of states, doping levels, and electron and phonon dispersions are given in Section S2 of SI [38]. For reproducibility, all information including input and output files, software, pseudopotentials, and additional details are provided on Materials Cloud Archive [40].

* jiaqi.zhou@uclouvain.be

† samuel.ponce@uclouvain.be

‡ jean-christophe.charlier@uclouvain.be

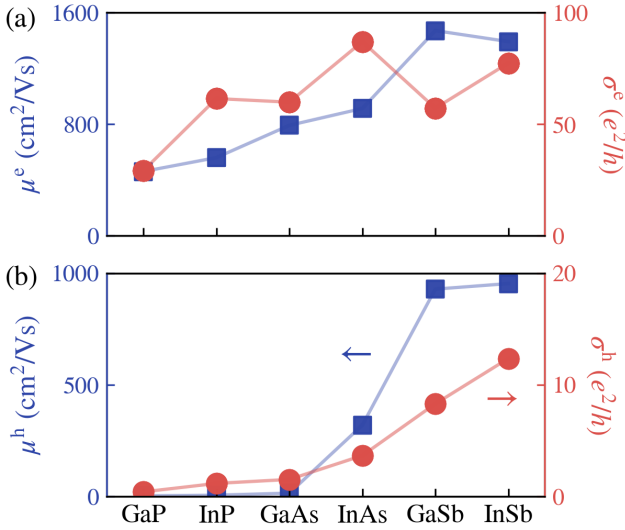


FIG. 1. Drift mobilities of pristine semiconductors and charge conductivities of doped systems for all the monolayers at 300 K. μ^e and μ^h denote (a) electron and (b) hole mobilities of pristine semiconductors with square markers (left axis), σ^e and σ^h indicate the conductivities of (a) electron-doped and (b) hole-doped systems with circle markers (right axis).

Charge transport – The phonon-limited charge conductivity in doped 2D semiconductor is calculated as [29]

$$\sigma_{\alpha\beta} = \frac{-e}{S^{\text{uc}}} \sum_n \int \frac{d^2k}{\Omega^{\text{BZ}}} v_{n\alpha} \partial_{E_\beta} f_{n\mathbf{k}}, \quad (1)$$

where α and β are Cartesian directions, S^{uc} is the unit cell area, Ω^{BZ} is the first Brillouin zone area, and $v_{n\alpha} = \hbar^{-1} \partial \varepsilon_{n\mathbf{k}} / \partial k_\alpha$ is the band velocity, n is the band index. The linear variation of the electronic occupation function $f_{n\mathbf{k}}$ in response to \mathbf{E} , $\partial_{E_\beta} f_{n\mathbf{k}}$, can be obtained by solving the Boltzmann transport equation with the scattering lifetime, see details in Eq. (S1) of SI [38]. The scattering rate, which is the inverse of scattering lifetime, is given as

$$\tau_{n\mathbf{k}}^{-1} = \frac{2\pi}{\hbar} \sum_{m\nu} \int \frac{d^2q}{\Omega^{\text{BZ}}} |g_{mn\nu}(\mathbf{k}, \mathbf{q})|^2 \times [(n_{q\nu} + 1 - f_{m\mathbf{k}+\mathbf{q}}^0) \delta(\varepsilon_{n\mathbf{k}} - \varepsilon_{m\mathbf{k}+\mathbf{q}} - \hbar\omega_{q\nu}) + (n_{q\nu} + f_{m\mathbf{k}+\mathbf{q}}^0) \delta(\varepsilon_{n\mathbf{k}} - \varepsilon_{m\mathbf{k}+\mathbf{q}} + \hbar\omega_{q\nu})], \quad (2)$$

where $g_{mn\nu}(\mathbf{k}, \mathbf{q})$ is the electron-phonon matrix element with phonon $\omega_{q\nu}$, $\varepsilon_{n\mathbf{k}}$ and $\varepsilon_{m\mathbf{k}+\mathbf{q}}$ are eigenvalues, $n_{q\nu}$ is the Bose-Einstein distribution. The drift mobility of pristine semiconductor is related to the charge conductivity as $\mu_{\alpha\beta} = \sigma_{\alpha\beta} / (e n^c)$ when the carrier density n^c is very small such that ionized impurity scattering can be neglected. The carrier mobilities are calculated considering quadrupole correction and Berry connection [28, 37]. Due to crystal symmetry, $\mu = \mu_{xx} = \mu_{yy}$, $\sigma = \sigma_{xx} = \sigma_{yy}$ in all the III-V monolayers. Note that μ and σ are separately calculated since the applied heavy dopings in this work break the linear relation between them [41].

The room-temperature mobilities of the pristine monolayers

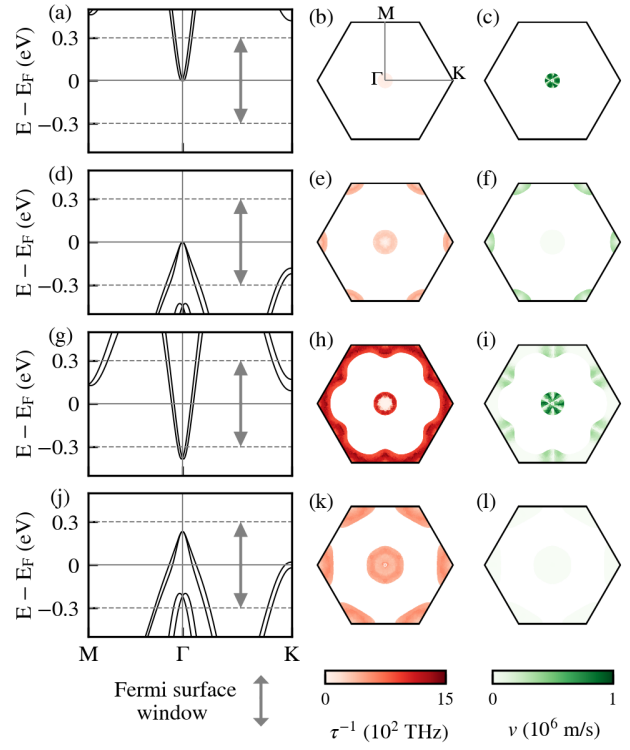


FIG. 2. Electronic structures, \mathbf{k} -resolved scattering rates $\sum_n \tau_{n\mathbf{k}}^{-1}$, and \mathbf{k} -resolved velocities $\sum_n v_{n\mathbf{k}}$ for (a)-(c) electron mobility and (d)-(f) hole mobility of pristine GaSb semiconductor, as well as for charge conductivities of (g)-(i) electron-doped and (j)-(l) hole-doped GaSb systems. Relevant Fermi surface windows are denoted by vertical arrows.

are presented in Fig. 1. All the materials exhibit high electron mobilities which are inversely proportional to their effective masses. It should be noted that μ^e of GaSb can reach up to $1470 \text{ cm}^2/\text{Vs}$, an exceptional value for a 2D semiconductor [21]. A much larger variation in the hole mobility is observed with values ranging from $10 \text{ cm}^2/\text{Vs}$ in phosphides to $953 \text{ cm}^2/\text{Vs}$ in antimonides. Interestingly, the two arsenides present quite different mobilities, while similar values are observed in the two phosphides and antimonides, respectively.

The transport behaviors can be intelligibly interpreted within the self-energy relaxation time approximation [29], where the mobility is inversely proportional to the scattering rate τ^{-1} and directly proportional to carrier velocity v . The electronic structures, \mathbf{k} -resolved scattering rates, and \mathbf{k} -resolved velocities of GaSb monolayer are presented as an example of the III-V monolayers. Figures 2(a)-(c) show that in the Fermi surface window of 0.3 eV for the electron mobility, the conduction band minimum (CBM) presents a Rashba splitting which is analogous to a single valley in the Brillouin zone. Hence, only intravalley scattering close to the Γ point is allowed, leading to low scattering rates under 100 THz . Besides, the sharp contour of bands produces high electron velocities around Γ . Both factors enable GaSb to present a high μ^e , which is also found in other III-V monolayers where CBMs always locate at Γ . In contrast, Figs. 2(d)-(f) show that the hole motion enables not only intravalley scatterings but also strong intervalley scatterings with a rate reaching up to 500 THz around K points. Moreover,

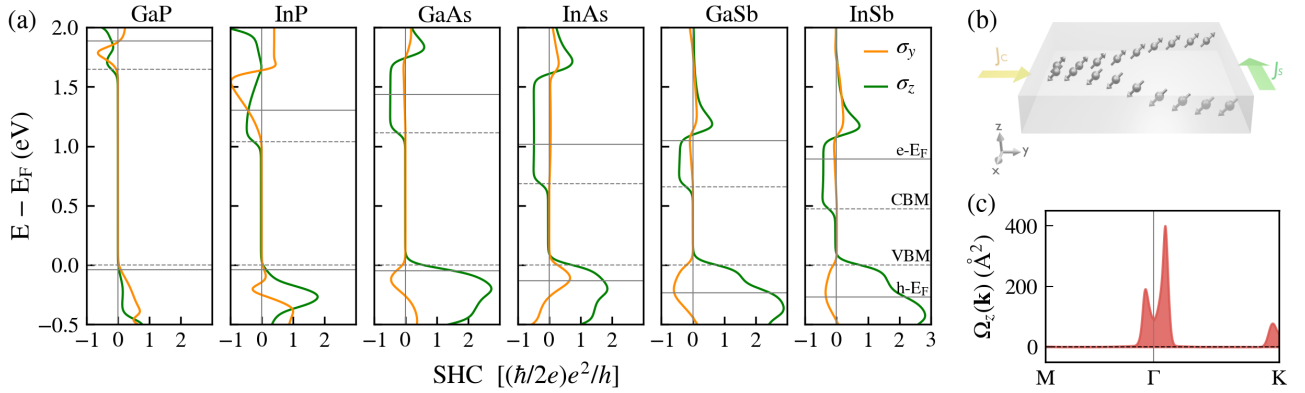


FIG. 3. (a) Energy-dependent spin Hall conductivities of all the pristine monolayers at 300 K. CBM and VBM of semiconductors are denoted by horizontal dashed lines, and the VBM is set as Fermi energy. Fermi energies of electron-doped and hole-doped systems are marked as e- E_F and h- E_F by horizontal solid lines. (b) Diagram of the spin Hall current with canted spin in the yz-plane. (c) Spin Berry curvature of GaSb at h- E_F .

the positions of valence band maximum (VBM) change with materials between Γ and K points: VBMs of antimonides are found at Γ , thus a relatively high μ^h can be achieved due to the suppressed intervalley scattering. The transition happens in arsenides where the VBMs of InAs and GaAs are located at Γ and K points, respectively. Therefore, the intervalley scattering around K reduces the hole mobility of GaAs, similarly in phosphides. The mode and spectral decompositions of scattering rates show that most of the scatterings are induced by the low-frequency out-of-plane acoustic mode in GaAs, while InAs is a Fröhlich-activated material where the dominant scattering originates from the high-frequency longitudinal optical mode. The \mathbf{k} -resolved scattering rates and velocities as well as spectral decompositions of all the materials are presented in Section S3 of SI [38]. Overall, despite belonging to the same III-V family, the hole mobility of these materials can vary significantly based on their electronic and vibrational properties.

Doping is a practical approach to tuning the transport properties of semiconductors [42]. Efficient screening is induced by heavy doping which turns semiconductors into metallic systems where SHE can occur. Considering the density of states, an electron doping of $1 \times 10^{13} \text{ cm}^{-2}$ and a hole doping of $2 \times 10^{13} \text{ cm}^{-2}$ are respectively applied to all the materials. The main impact of such doping is the shift of Fermi energy (E_F) by a few hundred meV, leaving the crystal structure and electronic bands nearly unaffected. Instead, the heavy doping yields a small phonon softening of the optical modes close to the zone center, suppressing the finite 2D slope in the long-wavelength limit. The charge conductivities of doped systems are shown in Fig. 1. The trend in doped conductivities is the same as that in pristine mobilities, except for the electron conduction in GaSb. The anomalous behavior of GaSb can be understood through the scattering and velocity mechanisms. Figures 2(g)-(i) show that the electron doping induces a shift of 0.38 eV of E_F , making eigenstates around M and K points closer to the Fermi surface, thus enabling a stronger scattering reaching up to 1400 THz. In addition, velocities around M and K points are limited by the large effective masses. Both factors limit the electron motion and reduce σ^e . The analyses above demonstrate that heavy doping can fundamentally alter the transport mechanisms, il-

lustrating the necessity to reconsider linear charge transport relation in these cases.

Spin Hall conductivity – SHC of 2D material, with spin current along x , electric field along y , and spin orientation along α direction ($\alpha = y$ or z), is calculated using Kubo formula [30]:

$$\sigma_\alpha = \frac{\hbar}{2e} \frac{e^2}{\hbar} \int_{BZ} \frac{d^2\mathbf{k}}{(2\pi)^2} \Omega_\alpha(\mathbf{k}), \quad (3)$$

where $\Omega_\alpha(\mathbf{k}) = \sum_n f_{n\mathbf{k}} \Omega_{\alpha,n}(\mathbf{k})$ is the spin Berry curvature, with the band-resolved spin Berry curvature as

$$\Omega_{\alpha,n}(\mathbf{k}) = \hbar^2 \sum_{m \neq n} \frac{-2 \text{Im}[\langle n\mathbf{k} | \hat{j}_\alpha | m\mathbf{k} \rangle \langle m\mathbf{k} | \hat{v}_y | n\mathbf{k} \rangle]}{(\varepsilon_{n\mathbf{k}} - \varepsilon_{m\mathbf{k}})^2}, \quad (4)$$

where $\hat{j}_\alpha = \frac{1}{2} \{ \hat{\sigma}_\alpha \hat{v}_x + \hat{v}_x \hat{\sigma}_\alpha \}$ is the spin current operator, $\hat{\sigma}_\alpha$ is the Pauli operator, \hat{v}_x and \hat{v}_y are velocity operators. Neumann's principle illustrates that the symmetries of physical property must include all the symmetries of the crystal [14]. Namely, the broken symmetries can remove the restrictions on SHC tensor [43, 44]. Apart from the conventional SHC σ_z , the lifted mirror symmetry \mathcal{M}_z enables another unconventional tensor element σ_y , while σ_x is prohibited by the preserved \mathcal{M}_x . The room-temperature σ_y and σ_z for all the pristine materials are presented in Fig. 3(a), and SHCs of doped systems are presented in Section S4 of SI [38], demonstrating that different from the case of charge conductivity, the major effect of doping on SHC is the shift of E_F . Due to the similarity, SHCs in electron- and hole-doped systems are respectively marked by e- E_F and h- E_F in Fig. 3(a). The electron-doped InP presents $\sigma_y^e \approx \sigma_z^e$, resulting in the canted spin orientation in yz-plane with a canted angle of 41° , as shown in Fig. 3(b). In arsenides and antimonides, σ_z^e is much larger than σ_y^e . The conduction bands of arsenides and antimonides produce a universal $\sigma_z^e = -0.5 (\hbar/2e)e^2/h$ around e- E_F , consistent with the literature which reports a universal SHC of $e/8\pi$ in the Rashba model [45]. Note that the difference between universal SHC values is caused by different constants used in Kubo formula. GaAs and InAs

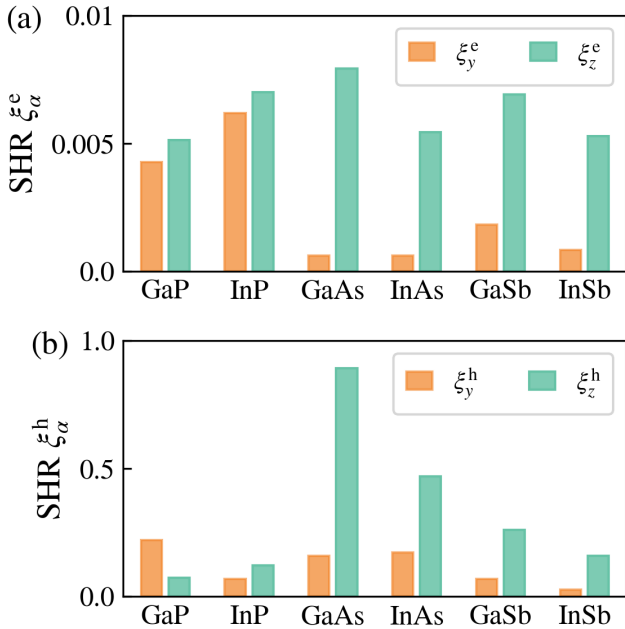


FIG. 4. Spin Hall ratios of all the monolayers doped by (a) electron and (b) hole. The subscripts indicate the results of two SHC tensor elements, σ_y and σ_z .

have the most robust σ_z^e over a large energy range since their conduction bands present a deep valley at the Γ point, while the interference of non-Rashba bands will break the universal SHC as observed in phosphides. We use a Rashba Hamiltonian to show that the universal SHC is robust against temperature once both Rashba bands are fully occupied, see details in Section S5 of SI [38]. Spin canted angles for all the materials can be found in Table S6 of SI [38].

In hole-doped systems, the strong spin-orbit splitting enhances both σ_y^h and σ_z^h . In most case, σ_z^h still dominates in SHC, and GaSb presents the largest $\sigma_z^h = 2.2 (\hbar/2e)e^2/h$. For comparison, MoS₂ monolayer exhibits $\sigma_z^h \approx 0.2 (\hbar/2e)e^2/h$, which is the only allowed SHC tensor component due to the constraint of high symmetry [17]. Figure 3(c) illustrates that in GaSb the spin Berry curvatures Ω_z predominantly originate from the region around Γ where spin-orbit splitting occurs and h-E_F locates inside the spin-orbit-splitting gap, see Fig. 2(j). In addition, the K point also makes contribution since h-E_F locates inside the splitting gap at K. The sign-invariant Ω_z results in a large SHC which is an integral of Ω_z over all the k-points. Spin textures and Ω_α decompositions of all the materials are presented in Section S6 of SI [38]. The discussions above manifest that the broken symmetry leads to the unconventional SHE, and doping can produce robust and large SHCs in III-V monolayers.

Spin Hall ratio – After obtaining the charge conductivities σ and spin Hall conductivities σ_α , the spin Hall ratio $\xi_\alpha = \frac{2e}{\hbar} |\frac{\sigma_\alpha}{\sigma}|$ can be discussed in the doped systems. Figure 4(a) shows that in the electron-doped systems, both ξ_y^e and ξ_z^e are less than 0.01 due to the high charge conductivity. In the case of hole doping, a few promising candidates are identified in Fig. 4(b). For the spin-y component, we find $\xi_y^h \approx 0.1$ in most

materials while the out-of-plane spin-z component varies much more between materials. Large σ_z^h are found in antimonides which also possess fairly large σ_z^h , thus limiting $\xi_z^h \approx 0.2$. In contrast, hole-doped arsenides are perfect candidates with high SHCs and low charge transports, yielding exceptional $\xi_z^h \approx 0.9$ and 0.5 in GaAs and InAs, respectively. Compared with heavy metals where $\xi \approx 0.01$ and where only conventional SHE is allowed, the hole-doped GaAs and other III-V monolayers exhibit great potential for low-power-consumption spintronic applications, since both large SHR and canted spin are crucial to realize field-free magnetization switching [16].

Experimental feasibility – Charge-to-spin conversion has been realized in MoS₂ and WSe₂ monolayers grown by chemical vapor deposition [13]. Since the first synthesis of 2D AlN layers by metal organic deposition [46], many efforts have been devoted to the synthesis of other 2D III-V materials [47, 48]. For example, GaSb films can be grown via a seeded lateral epitaxy, and the free-standing crystalline GaSb can be exfoliated from these films [49]. Moreover, 2D InAs flakes with high crystalline quality have been synthesized through van der Waals epitaxy with a thickness down to 4.8 nm [50]. Due to chemical similarity in one family, we expect similar techniques can be applied to the other III-V monolayers. Finally, the doping levels proposed in this work can be achieved via the advanced technique of electron beam in excess of $\pm 1 \times 10^{13} \text{ cm}^{-2}$ [51]. The doped state persists even after removing the electron beam and back-gate voltage, and the process is reversible and repeatable [51].

In conclusion, we compute the drift mobility, charge conductivity, spin Hall conductivity, and spin Hall ratio in III-V monolayers. Rashba splitting explains the exceptional electron mobilities in pristine semiconductors ranging from 461 to 1470 cm²/Vs, along with the high conductivities in the electron-doped regimes. The hole mobilities are much lower due to the intervalley scatterings, causing negligible charge conductivities in the hole-doped cases. For spin transport, the electron-doped systems exhibit a universal SHC, and the hole-doped systems present large values over $2 (\hbar/2e)e^2/h$ thanks to the strong spin-orbit splitting. Consequently, efficient charge-to-spin conversions can be realized in hole-doped systems, and an ultrahigh SHR $\xi_z^h \approx 0.9$ has been found in GaAs monolayer. Moreover, the broken symmetry of III-V monolayers allows for unconventional SHE where the spins are canted in the yz-plane. This work highlights the fascinating charge and spin transport characteristics of III-V monolayers and demonstrates their applicability in electronic and spintronic devices. The interplay between electronic and vibrational properties presented in this study could be used as a surrogate model to predict transport properties with enhanced spin Hall ratio via high-throughput calculations and machine learning.

Acknowledgment – The authors would like to thank Xi Dai, Matteo Giantomassi, Junfeng Qiao and Matthieu J. Verstraete for fruitful discussions. S. P. acknowledges the support from the Fonds de la Recherche Scientifique de Belgique (F.R.S.-FNRS). We acknowledge financial support from the European Union’s Horizon 2020 Research Project and Innovation Program-Graphene Flagship Core3 (No. 881603), from the Fédération Wallonie-Bruxelles through the ARC Grant (No. 21/26-116) and the EOS project “CONNECT” (No.

40007563), and from the Belgium F.R.S.-FNRS through the research project (No. T.029.22F). Computational resources have been provided by the PRACE award granting access to MareNostrum4 at Barcelona Supercomputing Center (BSC), Spain and Discoverer in SofiaTech, Bulgaria (OptoSpin project

ID. 2020225411), and by the Consortium des Équipements de Calcul Intensif (CÉCI), funded by the F.R.S.-FNRS under Grant No. 2.5020.11 and by the Walloon Region, as well as computational resources awarded on the Belgian share of the EuroHPC LUMI supercomputer.

[1] N. W. Ashcroft and N. D. Mermin, *Solid State Physics* (Harcourt College publisher, 1976).

[2] J. Sinova, S. O. Valenzuela, J. Wunderlich, C. H. Back, and T. Jungwirth, Spin Hall effects, *Rev. Mod. Phys.* **87**, 1213 (2015).

[3] A. Manchon, J. Železný, I. M. Miron, T. Jungwirth, J. Sinova, A. Thiaville, K. Garello, and P. Gambardella, Current-induced spin-orbit torques in ferromagnetic and antiferromagnetic systems, *Rev. Mod. Phys.* **91**, 035004 (2019).

[4] I. Žutić, J. Fabian, and S. Das Sarma, Spintronics: Fundamentals and applications, *Rev. Mod. Phys.* **76**, 323 (2004).

[5] K. Olejník, J. Wunderlich, A. C. Irvine, R. P. Campion, V. P. Amin, J. Sinova, and T. Jungwirth, Detection of electrically modulated inverse spin hall effect in an Fe/GaAs microdevice, *Phys. Rev. Lett.* **109**, 076601 (2012).

[6] X. Tao, Q. Liu, B. Miao, R. Yu, Z. Feng, L. Sun, B. You, J. Du, K. Chen, S. Zhang, L. Zhang, Z. Yuan, D. Wu, and H. Ding, Self-consistent determination of spin Hall angle and spin diffusion length in Pt and Pd: The role of the interface spin loss, *Sci. Adv.* **4**, eaat1670 (2018).

[7] M. Dc, R. Grassi, J.-Y. Chen, M. Jamali, D. Reifsnider Hickey, D. Zhang, Z. Zhao, H. Li, P. Quarterman, Y. Lv, M. Li, A. Manchon, K. A. Mkhoyan, T. Low, and J.-P. Wang, Room-temperature high spin-orbit torque due to quantum confinement in sputtered $\text{Bi}_x\text{Se}_{1-x}$ films, *Nat. Mater.* **17**, 800 (2018).

[8] N. H. D. Khang, Y. Ueda, and P. N. Hai, A conductive topological insulator with large spin Hall effect for ultralow power spin-orbit torque switching, *Nat. Mater.* **17**, 808 (2018).

[9] J. Zhou, J. Qiao, A. Bourrel, and W. Zhao, Intrinsic spin Hall conductivity of the semimetals MoTe_2 and WTe_2 , *Phys. Rev. B* **99**, 060408(R) (2019).

[10] B. Zhao, D. Khokriakov, Y. Zhang, H. Fu, B. Karpiak, A. Md. Hoque, X. Xu, Y. Jiang, B. Yan, and S. P. Dash, Observation of charge to spin conversion in Weyl semimetal WTe_2 at room temperature, *Phys. Rev. Res.* **2**, 013286 (2020).

[11] M. Vila, C.-H. Hsu, J. H. Garcia, L. A. Benítez, X. Waintal, S. O. Valenzuela, V. M. Pereira, and S. Roche, Low-symmetry topological materials for large charge-to-spin interconversion: The case of transition metal dichalcogenide monolayers, *Phys. Rev. Res.* **3**, 043230 (2021).

[12] P. Song, C.-H. Hsu, G. Vignale, M. Zhao, J. Liu, Y. Deng, W. Fu, Y. Liu, Y. Zhang, H. Lin, V. M. Pereira, and K. P. Loh, Coexistence of large conventional and planar spin Hall effect with long spin diffusion length in a low-symmetry semimetal at room temperature, *Nat. Mater.* **19**, 292 (2020).

[13] Q. Shao, G. Yu, Y.-W. Lan, Y. Shi, M.-Y. Li, C. Zheng, X. Zhu, L.-J. Li, P. K. Amiri, and K. L. Wang, Strong Rashba-Edelstein Effect-Induced Spin-Orbit Torques in Monolayer Transition Metal Dichalcogenide/Ferromagnet Bilayers, *Nano Lett.* **16**, 7514 (2016).

[14] R. E. Newnham, *Properties of Materials: Anisotropy, Symmetry, Structure* (Oxford University Press, Oxford, England, UK, 2005).

[15] A. Roy, M. H. D. Guimarães, and J. Sławińska, Unconventional spin hall effects in nonmagnetic solids, *Phys. Rev. Mater.* **6**, 045004 (2022).

[16] L. Liu, C. Zhou, X. Shu, C. Li, T. Zhao, W. Lin, J. Deng, Q. Xie, S. Chen, J. Zhou, R. Guo, H. Wang, J. Yu, S. Shi, P. Yang, S. Pennycook, A. Manchon, and J. Chen, Symmetry-dependent field-free switching of perpendicular magnetization, *Nat. Nanotechnol.* **16**, 277 (2021).

[17] W. Feng, Y. Yao, W. Zhu, J. Zhou, W. Yao, and D. Xiao, Intrinsic spin Hall effect in monolayers of group-VI dichalcogenides: A first-principles study, *Phys. Rev. B* **86**, 165108 (2012).

[18] T. Sohier, D. Campi, N. Marzari, and M. Gibertini, Mobility of two-dimensional materials from first principles in an accurate and automated framework, *Phys. Rev. Mater.* **2**, 114010 (2018).

[19] H. Wang, P. Gopal, S. Picozzi, S. Curtarolo, M. Buongiorno Nardelli, and J. Sławińska, Spin Hall effect in prototype Rashba ferroelectrics GeTe and SnTe, *npj Comput. Mater.* **6**, 1 (2020).

[20] J. Backman, Y. Lee, and M. Luisier, Electron-phonon calculations using a Wannier-based supercell approach: Applications to the monolayer MoS_2 mobility, *Solid-State Electron.* **198**, 108461 (2022).

[21] C. Zhang, R. Wang, H. Mishra, and Y. Liu, Two-Dimensional Semiconductors with High Intrinsic Carrier Mobility at Room Temperature, *Phys. Rev. Lett.* **130**, 087001 (2023).

[22] A. Cepellotti, J. Coulter, A. Johansson, N. S. Fedorova, and B. Kozinsky, Phoebe: a high-performance framework for solving phonon and electron Boltzmann transport equations, *J. Phys.: Mater.* **5**, 035003 (2022).

[23] F. Giustino, Electron-phonon interactions from first principles, *Rev. Mod. Phys.* **89**, 015003 (2017).

[24] W. Kohn, Nobel Lecture: Electronic structure of matter—wave functions and density functionals, *Rev. Mod. Phys.* **71**, 1253 (1999).

[25] S. Baroni, S. de Gironcoli, A. Dal Corso, and P. Giannozzi, Phonons and related crystal properties from density-functional perturbation theory, *Rev. Mod. Phys.* **73**, 515 (2001).

[26] N. Marzari, A. A. Mostofi, J. R. Yates, I. Souza, and D. Vanderbilt, Maximally localized Wannier functions: Theory and applications, *Rev. Mod. Phys.* **84**, 1419 (2012).

[27] G. Brunin, H. P. C. Miranda, M. Giantomassi, M. Royo, M. Stengel, M. J. Verstraete, X. Gonze, G.-M. Rignanese, and G. Hautier, Electron-Phonon beyond Fröhlich: Dynamical Quadrupoles in Polar and Covalent Solids, *Phys. Rev. Lett.* **125**, 136601 (2020).

[28] S. Poncé, M. Royo, M. Gibertini, N. Marzari, and M. Stengel, Accurate Prediction of Hall Mobilities in Two-Dimensional Materials through Gauge-Covariant Quadrupolar Contributions, *Phys. Rev. Lett.* **130**, 166301 (2023).

[29] S. Poncé, W. Li, S. Reichardt, and F. Giustino, First-principles calculations of charge carrier mobility and conductivity in bulk semiconductors and two-dimensional materials, *Rep. Prog. Phys.* **83**, 036501 (2020).

[30] J. Qiao, J. Zhou, Z. Yuan, and W. Zhao, Calculation of intrinsic spin Hall conductivity by Wannier interpolation, *Phys. Rev. B* **98**, 214402 (2018).

[31] S. Poncé, E. R. Margine, C. Verdi, and F. Giustino, EPW: Electron-phonon coupling, transport and superconducting properties using maximally localized Wannier functions, *Comput. Phys. Commun.* **209**, 116 (2016).

[32] H. Lee, S. Poncé, K. Bushick, S. Hajinazar, J. Lafuente-Bartolome, J. Leveillee, C. Lian, F. Macheda, H. Paudyal, W. H. Sio, M. Zacharias, X. Zhang, N. Bonini, E. Kioupakis, E. R. Margine, and F. Giustino, Electron-phonon physics from first principles using the EPW code, arXiv 10.48550/arXiv.2302.08085 (2023).

[33] G. Pizzi, V. Vitale, R. Arita, S. Blügel, F. Freimuth, G. Géranton, M. Gibertini, D. Gresch, C. Johnson, T. Koretsune, J. Ibañez-Azpiroz, H. Lee, J.-M. Lihm, D. Marchand, A. Marrazzo, Y. Mokrousov, J. I. Mustafa, Y. Nohara, Y. Nomura, L. Paulatto, S. Poncé, T. Ponweiser, J. Qiao, F. Thöle, S. S. Tsirkin, M. Wierzbowska, N. Marzari, D. Vanderbilt, I. Souza, A. A. Mostofi, and J. R. Yates, Wannier90 as a community code: new features and applications, *J. Phys.: Condens. Matter* **32**, 165902 (2020).

[34] P. Giannozzi, O. Andreussi, T. Brumme, O. Bunau, M. B. Nardelli, M. Calandra, R. Car, C. Cavazzoni, D. Ceresoli, M. Cococcioni, N. Colonna, I. Carnimeo, A. Dal Corso, S. de Gironcoli, P. Delugas, R. A. DiStasio, A. Ferretti, A. Floris, G. Fratesi, G. Fugallo, R. Gebauer, U. Gerstmann, F. Giustino, T. Gorni, J. Jia, M. Kawamura, H.-Y. Ko, A. Kokalj, E. Ktiçükbenli, M. Lazzeri, M. Marsili, N. Marzari, F. Mauri, N. L. Nguyen, H.-V. Nguyen, A. Otero-de-la Roza, L. Paulatto, S. Poncé, D. Rocca, R. Sabatini, B. Santra, M. Schlipf, A. P. Seitsonen, A. Smogunov, I. Timrov, T. Thonhauser, P. Umari, N. Vast, X. Wu, and S. Baroni, Advanced capabilities for materials modelling with Quantum ESPRESSO, *J. Phys.: Condens. Matter* **29**, 465901 (2017).

[35] X. Gonze, B. Amadon, G. Antonius, F. Arnardi, L. Baguet, J.-M. Beuken, J. Bieder, F. Bottin, J. Bouchet, E. Bousquet, N. Brouwer, F. Bruneval, G. Brunin, T. Cavignac, J.-B. Charraud, W. Chen, M. Côté, S. Cottenier, J. Denier, G. Geneste, P. Ghosez, M. Giantomassi, Y. Gillet, O. Gingras, D. R. Hamann, G. Hautier, X. He, N. Helbig, N. Holzwarth, Y. Jia, F. Jollet, W. Lafarge-Dit-Hauret, K. Lejaeghere, M. A. L. Marques, A. Martin, C. Martins, H. P. C. Miranda, F. Naccarato, K. Persson, G. Petretto, V. Planes, Y. Pouillon, S. Prokhorenko, F. Ricci, G.-M. Rignanese, A. H. Romero, M. M. Schmitt, M. Torrent, M. J. van Setten, B. Van Troeye, M. J. Verstraete, G. Zérah, and J. W. Zwanziger, The ABINIT project: Impact, environment and recent developments, *Comput. Phys. Commun.* **248**, 107042 (2020).

[36] T. Sohier, M. Calandra, and F. Mauri, Density functional perturbation theory for gated two-dimensional heterostructures: Theoretical developments and application to flexural phonons in graphene, *Phys. Rev. B* **96**, 075448 (2017).

[37] S. Poncé, M. Royo, M. Stengel, N. Marzari, and M. Gibertini, Long-range electrostatic contribution to electron-phonon couplings and mobilities of two-dimensional and bulk materials, *Phys. Rev. B* **107**, 155424 (2023).

[38] J. Zhou, S. Poncé, and J.-C. Charlier, Supplementary Information (2023).

[39] K. Wu, J. Chen, H. Ma, L. Wan, W. Hu, and J. Yang, Two-Dimensional Giant Tunable Rashba Semiconductors with Two-Atom-Thick Buckled Honeycomb Structure, *Nano Lett.* **21**, 740 (2021).

[40] J. Zhou, S. Poncé, and J.-C. Charlier, Materials Cloud Archive (2023).

[41] N. Ma and D. Jena, Charge Scattering and Mobility in Atomically Thin Semiconductors, *Phys. Rev. X* **4**, 011043 (2014).

[42] S. S. Awate, B. Mostek, S. Kumari, C. Dong, J. A. Robinson, K. Xu, and S. K. Fullerton-Shirey, Impact of large gate voltages and ultrathin polymer electrolytes on carrier density in electric-double-layer-gated two-dimensional crystal transistors, *ACS Appl. Mater. Interfaces* **15**, 15785 (2023).

[43] S. V. Gallego, J. Etxebarria, L. Elcoro, E. S. Tasci, and J. M. Perez-Mato, Automatic calculation of symmetry-adapted tensors in magnetic and non-magnetic materials: a new tool of the Bilbao Crystallographic Server, *Acta Crystallogr., Sect. A* **75**, 438 (2019).

[44] J. Zhou and J.-C. Charlier, Controllable spin current in van der Waals ferromagnet Fe_3GeTe_2 , *Phys. Rev. Res.* **3**, L042033 (2021).

[45] J. Sinova, D. Culcer, Q. Niu, N. A. Sinitsyn, T. Jungwirth, and A. H. MacDonald, Universal Intrinsic Spin Hall Effect, *Phys. Rev. Lett.* **92**, 126603 (2004).

[46] W. Wang, Y. Zheng, X. Li, Y. Li, H. Zhao, L. Huang, Z. Yang, X. Zhang, and G. Li, 2D AlN Layers Sandwiched Between Graphene and Si Substrates, *Adv. Mater.* **31**, 1803448 (2019).

[47] F. Lu, H. Wang, M. Zeng, and L. Fu, Infinite possibilities of ultrathin III-V semiconductors: Starting from synthesis, *iScience* **25**, 103835 (2022).

[48] A. Nikolaevich Klochkov, A. Nikolaevich Vinichenko, A. Alekseevich Samolyga, S. Mihailovich Ryndya, M. Viktorovich Poliakov, N. Ivanovich Kargin, and I. Sergeevich Vasil'evskii, Growth by molecular beam epitaxy and characterization of n-InAs films on sapphire substrates, *Appl. Surf. Sci.* **619**, 156722 (2023).

[49] S. Manzo, P. J. Strohbeen, Z. H. Lim, V. Saraswat, D. Du, S. Xu, N. Pokharel, L. J. Mawst, M. S. Arnold, and J. K. Kawasaki, Pinhole-seeded lateral epitaxy and exfoliation of GaSb films on graphene-terminated surfaces, *Nat. Commun.* **13**, 1 (2022).

[50] J. Dai, T. Yang, Z. Jin, Y. Zhong, X. Hu, J. Zou, W. Xu, T. Li, Y. Lin, X. Zhang, and L. Zhou, Controlled growth of two-dimensional InAs single crystals via van der Waals epitaxy, *Nano Res.* **15**, 9954 (2022).

[51] W. Shi, S. Kahn, N. Leconte, T. Taniguchi, K. Watanabe, M. Crommie, J. Jung, and A. Zettl, High-Order Fractal Quantum Oscillations in Graphene/BN Superlattices in the Extreme Doping Limit, *Phys. Rev. Lett.* **130**, 186204 (2023).